J. Fluid Mech. (1994), *vol.* 265, *pp.* 265–288

Axisymmetric unsteady Stokes flow past an oscillating finite-length cylinder

By MICHAEL LOEWENBERG†
Department of Physical Chemistry, University of Sydney, NSW, 2006, Australia

(Received 15 July 1993 and in revised form 1 November 1993)

The flow field generated by axial oscillations of a finite-length cylinder in an incompressible viscous fluid is described by the unsteady Stokes equations and computed with a first-kind boundary-integral formulation. Numerical calculations were conducted for particle oscillation periods comparable with the viscous relaxation time and the results are contrasted to those for an oscillating sphere and spheroid. For high-frequency oscillations, a two-term boundary-layer solution is formulated that involves two, sequentially solved, second-kind integral equations. Good agreement is obtained between the boundary-layer solution and fully numerical calculations at moderate oscillation frequencies. The flow field and traction on the cylinder surface display several features that are qualitatively distinct from those found for smooth particles. At the edges, where the base joins the side of the cylinder, the traction on the cylinder surface exhibits a singular behaviour, characteristic of steady two-dimensional viscous flow. The singular traction is manifested by a sharply varying pressure profile in a near-field region. Instantaneous streamline patterns show the formation of three viscous eddies during the decelerating portion of the oscillation cycle that are attached to the side and bases of the cylinder. As deceleration proceeds, the eddies grow, coalesce at the edges of the particle, and thus form a single eddy that encloses the entire particle. Subsequent instantaneous streamline patterns for the remainder of the oscillation cycle are insensitive to particle geometry: the eddy diffuses outwards and vanishes upon particle reversal; a simple streaming flow pattern occurs during particle acceleration. The evolution of the viscous eddies is most apparent at moderate oscillation frequencies. Qualitative results are obtained for the oscillatory flow field past an arbitrary particle. For moderate oscillation frequencies, pathlines are elliptical orbits that are insensitive to particle geometry; pathlines reduce to streamline segments in constant-phase regions close to and far from the particle surface.

1. Introduction

The oscillatory motion of microscopic particles in a Newtonian viscous liquid arises in several scientific and engineering applications. The swimming motion of micro-organisms and Brownian particle motion are well-known natural examples (Hocquart & Hinch 1983; Hurd *et al.* 1985). Ultrasonic (Allegra & Hawley 1971), and more recently, electroacoustic (O'Brien 1990) devices rely on a knowledge of oscillatory motion to relate macroscopic measurements to microscopic suspension parameters. The latter application exploits the reciprocity between oscillating electric and pressure fields in colloidal suspensions that interact via the electrophoretic mobility of a colloidal particle.

† Current address: Department of Chemical Engineering, University of Colorado, Boulder, CO 80309-0424, USA.

For oscillatory motion, the particle velocity is described by $U_0 \boldsymbol{e} \cos \omega t$, where $\boldsymbol{e}$ and U_0/ω are the direction and magnitude of the particle displacement. In general, the Navier–Stokes equations govern the fluid motion. In most situations of interest, the particle displacement is very small compared to particle size, a, herein taken to be the cylinder or sphere radius. It follows that the Strouhal number is large: $Sl = \omega a/U_0 \gg 1$. In electroacoustic applications (O'Brien 1990; Loewenberg & O'Brien 1992) for example, $U_0 \sim 10^{-3}$ cm s^{-1}, and $\omega \sim 1$ MHz thus, $Sl \sim 10^5$ for a 1 μm particle; the particle motion is merely an ultrasonic 'buzzing': indeed, particle displacement is exceedingly small compared to particle size. It follows that the Reynolds number based on particle size is small (Batchelor 1967): $Re = U_0 a/\nu = |\lambda|^2/Sl \ll 1$, where ν is the kinematic viscosity of the suspending fluid, and $|\lambda|$ is an $O(1)$ frequency parameter defined beneath (1.1). This scaling result allows the Navier–Stokes equations to be linearized, which greatly simplifies theoretical analyses of microscopic oscillatory particle motion (Kim & Karrila 1991). The fluid can be considered incompressible if the sonic wavelength is large compared to the particle size at the oscillation frequency, ω (Batchelor 1967). This is generally true at the frequencies of interest; for example, the wavelength of sound in water is 1 cm at the typical frequency, $\omega = 1$ MHz.

It follows that the unsteady Stokes equations govern the fluid velocity and pressure:

$$\nabla \cdot \boldsymbol{\sigma}(\boldsymbol{x}) = \lambda^2 \boldsymbol{u}(\boldsymbol{x}), \quad \nabla \cdot \boldsymbol{u}(\boldsymbol{x}) = 0; \quad \sigma_{ij} = \left[\frac{\partial u_i}{\partial x_j} + \frac{\partial u_j}{\partial x_i}\right] - \delta_{ij} p, \tag{1.1}$$

which have been non-dimensionalized using U_0 and $\mu U_0/a$ (μ is the dynamic viscosity) for the characteristic velocity and pressure; σ_{ij} is the viscous stress tensor. The complex-valued frequency parameter, $\lambda = a(\omega/\nu)^{\frac{1}{2}} e^{-i\pi/4}$, characterizes the unsteadiness of the fluid motion; $|\lambda|^2$ is the ratio of the viscous relaxation time to the period of particle oscillation, and $|\lambda|^{-1}$ is the distance that vorticity diffuses during half an oscillation cycle: the viscous penetration length, normalized by the particle size.

Without loss of generality, $\boldsymbol{u}(\boldsymbol{x}, t) = \boldsymbol{u}(\boldsymbol{x}) e^{-i\omega t}$ and $p(\boldsymbol{x}, t) = p(\boldsymbol{x}) e^{-i\omega t}$ have been assumed in (1.1), where $\boldsymbol{u}(\boldsymbol{x})$ and $p(\boldsymbol{x})$ are, in general, complex-valued fields. By the linearity of the unsteady Stokes equations, general time-dependent behaviour can be constructed from its Fourier components (Basset 1888; Lawrence & Weinbaum 1988). It follows that unsteady Stokes flow is reversible which precludes net particle motion and inertial steady-streaming flow (Batchelor 1967); pathlines for the fluid motion are closed orbits.

The solution of (1.1) must satisfy a no-slip boundary condition, $\boldsymbol{u} = \boldsymbol{e}$, on the particle surface, and on the assumption that the particle is isolated, $\boldsymbol{u}$ and p must vanish at infinity. The steady Stokes equations are recovered from (1.1) for $|\lambda| \ll 1$; at high oscillation frequencies, $|\lambda| \gg 1$, the fluid motion is described by potential flow everywhere except within a viscous boundary layer on the particle surface that has thickness $|\lambda|^{-1}$. Under typical conditions relevant to the applications cited above, $|\lambda| = O(1)$; e.g. $|\lambda| = 1$ for a 1 μm particle in water with $\omega = 1$ MHz.

The detailed effects of particle shape in steady Stokes flow are, by now, well-known thanks to extensive studies on the subject (e.g. Oberbeck 1876; Edwardes 1892; Jeffery 1922; Burgers 1938). By contrast, oscillatory Stokes flow past a microscopic particle has received far less attention. Beginning with the investigation on the oscillatory motion of a sphere or (infinite) cylinder in a viscous fluid by Stokes (1851), most investigations on oscillatory Stokes flow past particles have been focused on finding the frequency-dependent resistance of the particle. It has been shown that the unsteady hydrodynamic resistance of moderate-aspect-ratio spheroids (Lawrence & Weinbaum 1988; Pozrikidis 1989*a*) and cylinders (Loewenberg 1993) is accurately approximated

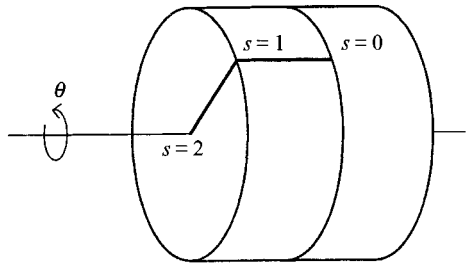

FIGURE 1. Defining sketch showing the meridian-plane contour, $0 \leqslant s \leqslant 2$. The cylinder centreline is defined by $s = 0$, $s = \pm 1$ on the cylinder edges, and the symmetry axis intersects the particle surface at $s \pm 2$; θ is the azimuthal angle.

($\pm 5\%$) at all frequencies by an algebraic expression involving only the steady Stokes resistance, added mass, and Basset force of a particle which are determined from the steady Stokes and potential flow equations.

There have been virtually no investigations into the details of the oscillatory flow field past a particle. An exception is the investigation of Pozrikidis (1989*b*) on the oscillatory flow field past spheroids, dumbbells, and biconcave discs that was motivated by an interest in microscopic convective processes such as blood flow. Numerical solutions were obtained using a boundary integral formulation of the unsteady Stokes equations. Tangential stress distributions exhibited the largest phase angles on the portions of the particle surface with the least curvature, and the smallest phase angle on highly curved portions. Since vanishing tangential stress signals locally reversing flow, Pozrikidis (1989*b*) argued that reversal occurs first on surface regions of lowest curvature; reversal is last on highly curved regions. This feature implies the existence of travelling stagnation points on the spheroid surface that are associated with the formation of an attached eddy on the low-curvature portion of the surface. The eddy gradually expands until it encloses the entire particle surface and then detaches. Streamline patterns were computed at different instants throughout the oscillation cycle to illustrate the transient flow field. Unfortunately, streamline patterns could not be constructed to illustrate the attached eddy. The streamline patterns that were shown for oscillating spheroids, dumbbells, and biconcave discs were qualitatively the same as those for an oscillating sphere.

Finite-length circular cylinders in potential flow (Hess 1962) and steady Stokes flow (Gluckman, Weinbaum & Pfeffer 1972; Youngren & Acrivos 1975; Chen, Leu & Zargar 1986) have been the subject of several well-known theoretical studies since the advent of computational fluid mechanics around 1960. In each case a cylindrical particle was studied, in part because of the flow field or traction singularity that is predicted by two-dimensional flow theories (Dean & Montagnon 1949; Jackson 1962) to occur at the sharp edges formed where the flat bases join the circular side of the cylinder (cf. figure 1). For numerical computations, a finite-length cylinder is the simplest three-dimensional geometry with sharp features because of its axisymmetry and fore-aft symmetry. Furthermore, numerical calculations for certain hydrodynamic resistance functions can be empirically tested because cylindrical particles are a practical shape for experiments: they are relatively easy to manufacture (Heiss & Coull 1952; Ui, Hussey & Roger 1984; Kasper, Niida & Yang 1985; Davis 1991).

The purpose of this paper is to examine the detailed effects of a non-smooth particle profile on unsteady Stokes flow. These effects are investigated for case of an axially oscillating finite-length circular cylinder with a diameter equal to its height as illustrated in figure 1; a unit aspect-ratio cylinder was chosen to emphasize effects of

the edges on the flow field. The results of this investigation provide a deeper general understanding of oscillatory Stokes flow. The general capability of the boundary integral formulation for numerically solving the unsteady Stokes equations is made more apparent.

In §2, the boundary integral formulation of the unsteady Stokes equations is developed. A boundary-layer solution is formulated for high oscillation frequencies. In §3, the numerical solution procedure is described. In §4, numerical results for the traction on the surface of an oscillating cylinder are presented and discussed; results are contrasted with the analytical results for a sphere and numerical results for spheroids. The boundary-layer solution verifies the consistency of the numerical solutions. In §5, numerical solutions are presented for the fluid velocity and pressure fields past an oscillating cylinder, and the results are contrasted with those for spheres and spheroids. Contour plots are used to depict the pressure field, streamline plots show the fluid velocity at several critical instants during the particle oscillation cycle, and pathline plots reveal the displacement of fluid elements during a complete cycle. Concluding remarks are made in §6.

2. Boundary integral formulation

2.1. *General formulation for a translating particle*

Numerical solutions of the unsteady Stokes equations (1.1) were obtained using a boundary integral formulation. The relevant theory is well-established for the steady Stokes equations (Ladyzhenskaya 1969) and has been recently adapted for unsteady flows (Pozrikidis 1989*b*, 1992; Kim & Karrila 1991). The development is summarized below for linearized incompressible flow (potential flow, and steady and unsteady Stokes flow) past a translating, rigid particle in a quiescent fluid.

An integral expression for the fluid velocity at a point $\boldsymbol{x}_0$ in the flow field is obtained starting with the reciprocal relation for unsteady Stokes flow: $\nabla\cdot[\boldsymbol{u}(\boldsymbol{x})\cdot\boldsymbol{\sigma}^*(\boldsymbol{x})-\boldsymbol{u}^*(\boldsymbol{x})\cdot\boldsymbol{\sigma}(\boldsymbol{x})]=0$, where $\boldsymbol{u},\boldsymbol{\sigma}$ and $\boldsymbol{u}^*,\boldsymbol{\sigma}^*$ are solutions of (1.1) at $\boldsymbol{x}$. Then we take $\boldsymbol{u}^*$, $\boldsymbol{\sigma}^*=\boldsymbol{S},\boldsymbol{T}$ which vanish at infinity and satisfy the singular, unsteady Stokes equations:

$$\frac{\partial T_{ikj}}{\partial \hat{x}_k}-\lambda^2 S_{ij}=-8\pi\delta_{ij}\,\delta(\hat{\boldsymbol{x}}),\quad \frac{\partial S_{ij}}{\partial \hat{x}_i}=0, \tag{2.1}$$

where δ_{ij} and $\delta(\hat{\boldsymbol{x}})$ are the Kronecker and Dirac delta functions, and $\hat{\boldsymbol{x}}=\boldsymbol{x}-\boldsymbol{x}_0$. The desired expression is obtained from a limiting process where $\boldsymbol{x}_0$ is excluded from the domain by a ball of vanishing radius:

$$u_j(\boldsymbol{x}_0)=-\frac{1}{8\pi}\int_{S_P}[\sigma_{ik}(\boldsymbol{x})\,S_{ij}(\hat{\boldsymbol{x}})-u_i(\boldsymbol{x})\,T_{ikj}(\hat{\boldsymbol{x}})]\,n_k(\boldsymbol{x})\,\mathrm{d}S(\boldsymbol{x}), \tag{2.2}$$

where S_P is the particle surface with outward normal n_k. For $\boldsymbol{x}_0$ on S_P, the factor $1/8\pi$ in (2.2) becomes $1/4\pi$. The unsteady Stokeslet, S_{ij}, and associated stress and pressure fields, T_{ikj} and Q_j, are (Williams 1966):

$$S_{ij}(\boldsymbol{x})=2\mathrm{e}^{-\lambda r}\left[a(\lambda r)\frac{\delta_{ij}}{r}-b(\lambda r)\frac{\hat{x}_i\hat{x}_j}{r^3}\right]-\frac{1}{\lambda^2}\frac{\partial Q_j(\hat{\boldsymbol{x}})}{\partial x_i}, \tag{2.3a}$$

$$T_{ikj}=\left[\frac{\partial S_{ij}}{\partial \hat{x}_k}+\frac{\partial S_{kj}}{\partial \hat{x}_i}\right]-\delta_{ik}\,Q_j,\quad Q_j(\hat{\boldsymbol{x}})=2\frac{\hat{x}_j}{r^3}, \tag{2.3b, c}$$

where

$$a(t)=1+\frac{1}{t}+\frac{1}{t^2},\quad b(t)=1+\frac{3}{t}+\frac{3}{t^2},$$

and $r = |\hat{\boldsymbol{x}}|$. As indicated, S_{ij} is symmetric, and T_{ikj} is symmetric with respect to the first two indices only.

Using the divergence theorem and (2.1), we can rewrite (2.3) for a translating particle as (Pozrikidis 1989*b*)

$$u_j(\boldsymbol{x}_0) = -\frac{1}{8\pi}\int_{S_P} f_i(\boldsymbol{x})\, S_{ij}(\hat{\boldsymbol{x}})\, \mathrm{d}S(\boldsymbol{x}), \tag{2.4}$$

where $f_i + \lambda^2 (e_k x_k) n_i = \sigma_{ik} n_k$ is the traction on the particle surface. It does not seem possible to eliminate the associated stress field, T_{ikj}, in (2.3) by similar manoeuvers and obtain an analogous expression for rotary motion except when $\lambda = 0$ (Kim & Karrila 1991). The (symmetric) oscillatory hydrodynamic resistance, defined by $F_i = -\mu a U_0 e_j \,\mathrm{Re}\{R_{ij} \mathrm{e}^{-\mathrm{i}\omega t}\}$, is

$$R_{ij} = -e_i \int_{S_P} f_j \,\mathrm{d}S - \lambda^2 V_P \delta_{ij}, \tag{2.5}$$

where V_P is the dimensionless particle volume and $\lambda^2 V_P \delta_{ij}$ is the resistance due to buoyancy.

Substituting (2.4) into the unsteady Stokes equations (1.1), and using (2.1), yields the pressure field at points away from the particle boundary (Ladyzhenskaya 1969):

$$p(\boldsymbol{x}_0) = -\frac{1}{8\pi}\int_{S_P} f_i(\boldsymbol{x})\, Q_i(\hat{\boldsymbol{x}})\, \mathrm{d}S(\boldsymbol{x}), \tag{2.6}$$

where the factor $1/8\pi$ is replaced by $1/4\pi$ for $\boldsymbol{x}_0$ on S_P. The result applies for all linearized incompressible flows because $\nabla^2 p(\boldsymbol{x}_0) = 0$, as implied by (1.1). Equation (2.4) applies for $\boldsymbol{x}_0$ in the fluid or on the particle surface where $u_j = e_j$:

$$e_j = -\frac{1}{8\pi}\int_{S_P} f_i(\boldsymbol{x})\, S_{ij}(\hat{\boldsymbol{x}})\, \mathrm{d}S(\boldsymbol{x}), \tag{2.7}$$

which is a first-hand Fredholm-type integral equation for the modified traction, $f_i = \sigma_{ik} n_k - \lambda^2 (x_k e_k) n_i$.

For $\lambda \to 0$, the modified and true tractions coincide, and the steady Stokeslet is recovered from (2.3): $S_{ij} \to \delta_{ij}/r + \hat{x}_i \hat{x}_j / r^3$; thus, (2.7) reduces to the boundary integral equation for the steady Stokes traction (Ladyzhenskaya 1969). For $|\lambda| \ll 1$, the translational resistance tensor is (Pozrikidis 1989*b*)

$$R_{ij} = R^0_{ij} + \lambda R^0_{ik} R^0_{kj}/6\pi + O(|\lambda|^2), \tag{2.8}$$

where R^0_{ij} is the steady Stokes resistance tensor.

2.2. *Asymptotic solution for high-frequency oscillation*

As discussed in §3, it is difficult to solve (2.7) for $|\lambda| \gg 1$. The asymptotic high-frequency solution, formulated below, is therefore useful. At moderately high frequencies, the asymptotic solution provides a test of the fully numerical solutions.

2.2.1. *Potential flow field*

In the high-frequency limit, $|\lambda| r \to \infty$, viscous terms in the singularity solution (2.3) vanish exponentially; the singular velocity and stress field describe the irrotational flow associated with a potential dipole:

$$S_{ij} = -\frac{1}{\lambda^2}\frac{\partial Q_j}{\partial \hat{x}_i}, \quad T_{ikj} = -\delta_{ik} Q_j, \tag{2.9}$$

where the singular pressure, Q_j, is given by (2.2c). Thus, in the limit $|\lambda| r \to \infty$, (2.4) becomes

$$\Phi(\boldsymbol{x}_0) = -\frac{1}{8\pi\lambda^2}\int_{S_P} f_i(\boldsymbol{x})\, Q_i(\hat{\boldsymbol{x}})\, \mathrm{d}S(\boldsymbol{x}), \tag{2.10}$$

for $\boldsymbol{x}_0$ in the flow field where Φ is a velocity potential that satisfies:

$$u_j = -\frac{\partial \Phi}{\partial x_j}, \quad \nabla^2\Phi = 0, \quad \sigma_{ik} = -\lambda^2\Phi\delta_{ik}. \tag{2.11}$$

It follows that $f_i = -\lambda^2[\Phi + e_k x_k] n_i$; inserting this result into (2.10), and allowing $\boldsymbol{x}_0$ to approach S_P, yields a second-kind Fredholm-type integral equation for the velocity potential on the particle surface:

$$\Phi(\boldsymbol{x}_0) - e_k x_k = -\frac{1}{4\pi}\int_{S_P} [\Phi(\boldsymbol{x}) + e_k x_k]\, Q_i\, n_i\, \mathrm{d}S(\boldsymbol{x}), \tag{2.12}$$

where the factor of $1/4\pi$ becomes $1/8\pi$ for points away from the particle surface.

The resulting irrotational velocity field vanishes at infinity and satisfies impenetrability on the particle surface but it fails to satisfy the no-slip boundary condition on the particle surface. This familiar problem results from the non-uniform limiting process, $|\lambda| r \to \infty$, used to derive (2.10) from (2.4). At high frequencies, a viscous boundary layer of thickness $|\lambda|^{-1}$ resides on the particle surface. Away from the boundary layer, the velocity field is described by (2.12) because the limit, $|\lambda| r \to \infty$, is uniformly attained. For the linearized flow considered herein that describes small-amplitude oscillations, boundary-layer separation does not occur (Batchelor 1967).

2.2.2. *Boundary-layer solution*

In the viscous boundary layer on the particle surface, the characteristic length for tangential flow field variations is the local radius of mean curvature, $b(\boldsymbol{x})$, whereas flow field variations normal to the particle surface occur on a lengthscale, $|\lambda|^{-1}$. For $|\lambda|\, b(\boldsymbol{x}) \gg 1$, the boundary-layer equations for the unsteady Stokes flow field are

$$\frac{\partial^2 \boldsymbol{w}}{\partial z^2} - \lambda^2 \boldsymbol{w} = \lambda^2 \nabla_S \Phi, \quad \frac{\partial^2 v}{\partial z^2} - \lambda^2 v = \frac{\partial p}{\partial z}, \quad \nabla_S \cdot \boldsymbol{w} + \frac{\partial v}{\partial z} = 0, \tag{2.13a–c}$$

where $\boldsymbol{w}$ is the tangential velocity field, v is the normal velocity component, z is the local normal coordinate, ∇_S is the surface gradient operator and Φ is the velocity potential (evaluated at the particle surface) for the flow field outside the boundary layer.† The velocity field that satisfies the no-slip boundary condition on the particle surface and matches the potential flow solution, (2.12), outside of the boundary layer is

$$\boldsymbol{w} = \boldsymbol{u}' \mathrm{e}^{-\lambda z} - \nabla_S \Phi, \quad v = -\frac{1}{\lambda}\nabla_S \cdot \boldsymbol{u}'(1 - \mathrm{e}^{-\lambda z}) - \frac{\partial \Phi}{\partial n}, \quad \frac{\partial p'}{\partial n} = \nabla_S \cdot \boldsymbol{u}', \tag{2.14a–c}$$

where $\boldsymbol{u}' = \boldsymbol{e} + \nabla\Phi$ is the associated tangential slip velocity (relative to the particle surface), and $\lambda p' = p - \lambda^2\Phi$ is the $O(|\lambda|)$ excess pressure that results from the boundary layer flow.

† Equation (2.13a) is misprinted in Loewenberg (1994, Equation 10a).

For $|\lambda| \gg 1$, the traction on the particle surface is

$$f_i = -\lambda^2 \Phi n_i + \lambda f_i', \tag{2.15}$$

where $\lambda^2\Phi$ is the leading-order pressure distribution on the particle surface obtained from the potential flow field (2.12); $\lambda f_i'$ is an $O(|\lambda|)$ correction associated with the boundary-layer solution:

$$f_i' = u_i' - p' n_i, \tag{2.16}$$

where $\lambda u_i'$ is the leading-order tangential stress, obtained by differentiating the potential flow solution; $\lambda p'$ is the $O(|\lambda|)$ correction to the leading-order pressure distribution.

For $\boldsymbol{x}_0$ on S_P, (2.6) yields a second-kind Fredholm-type integral equation for the excess pressure:

$$p'(\boldsymbol{x}_0) = -\frac{1}{4\pi} \int_{S_P} f_i'(\boldsymbol{x})\, Q_i(\hat{\boldsymbol{x}})\, \mathrm{d}S(\boldsymbol{x}),$$

where (2.12) must first be solved to supply the slip velocity, u_i'. Unfortunately, the integral of $u_i'(\boldsymbol{x})\, Q_i(\hat{\boldsymbol{x}})$ on S_P is only conditionally convergent because its r^{-2} singularity makes numerical integration difficult. A better numerical procedure is obtained by incorporating (2.14*c*) and the fact that $\nabla^2 p'(\boldsymbol{x}_0) = 0$; accordingly, a well-posed second-kind integral equation is given by (Jackson 1962)

$$p'(\boldsymbol{x}_0) = -\frac{1}{4\pi} \int_{S_P} \left[\frac{2}{r} \nabla_S \cdot \boldsymbol{u}'(\boldsymbol{x}) + p'(\boldsymbol{x})\, Q_i(\hat{\boldsymbol{x}})\, n_i \right] \mathrm{d}S(\boldsymbol{x}), \tag{2.17}$$

where $\boldsymbol{u}'$ is obtained from (2.12).

At high oscillation frequencies, the translational resistance is (Batchelor 1967)

$$R_{ij} = \lambda^2 M_{ij}^A + \lambda B_{ij}^\infty + O(1), \tag{2.18}$$

where $$M_{ij}^A = e_i \int_{S_P} \Phi n_j \,\mathrm{d}S \quad \text{and} \quad \lambda B_{ij}^\infty = e_i \int_{S_P} f_j' \,\mathrm{d}S$$

are the symmetric (Gavze 1990) added mass and Basset force tensors. As indicated, the added mass is obtained from the potential flow solution. The Basset force tensor is the leading-order correction that results from the boundary-layer solution but it can also be obtained from the potential flow solution by considering viscous dissipation in the boundary layer (Batchelor 1967):

$$B_{ij}^\infty = e_i e_j \int_{S_P} u_k' u_k' \,\mathrm{d}S.$$

The boundary-layer solution is considered herein because the pointwise traction is of interest.

3. Numerical solution procedure

For the axisymmetric flow past an oscillating cylinder, the modified surface traction, $f_i = \sigma_{ik} n_k - \lambda^2 (x_k e_k) n_i$, has a normal and tangent component; both are axisymmetric. The tangential component has fore-aft symmetry, the normal component is fore-aft

antisymmetric. The symmetry properties of the velocity potential, Φ, and excess pressure coefficient, p', are the same as $f_i n_i$. Thus, $f_i(\boldsymbol{x})$, and the high-frequency boundary-layer contribution, $f_i'(\boldsymbol{x})$, are determined everywhere on the particle surface by their values on the one-dimensional, meridian-plane contour depicted in figure 1.

Numerical solutions of (2.7), (2.12), and (2.17) were obtained by discretizing the contour, $0 \leqslant s \leqslant 2$, (cf. figure 1) into $2N$ unequal segments $\Delta s_\alpha = t_\alpha - t_{\alpha-1}, \alpha = 1, 2, 3, \ldots, 2N$ (N segments on each subinterval: $[0,1]$ and $[1,2]$), with centres, $s_\alpha = \frac{1}{2}(t_\alpha + t_{\alpha-1})$, where $t_\alpha = 1 - [(N-\alpha)|N-\alpha|^{m/1-m}]N^{1/m-1}$. This procedure yields $\Delta s_\alpha = O(|s_\alpha - 1|^m/N)$. The corresponding unknown functions $f_i(s)$, $\Phi(s)$, and $p'(s)$ were approximated by piecewise-constant functions $f_i(s_\alpha)$, $\Phi(s_\alpha)$, and $p'(s_\alpha)$ on the contour segments.

As discussed in §4, the flow around a 90° two-dimensional corner has an algebraically singular traction: $|f_i(s)| \propto |s-1|^{-0.455516\ldots}$ for steady, viscous flow, and $|f_i'(s)| \propto |s-1|^{-\frac{1}{3}}$ for the boundary-layer flow. It will be shown that the local flow field near the cylinder edge is characterized by quasi-steady two-dimensional flow. Anticipating these results, the above discretization procedure was implemented with $m \approx \frac{1}{2}$ for numerical solutions of (2.7) ($|\lambda| = O(1)$), and with $m = \frac{1}{3}$ for (2.12) and (2.17) ($|\lambda| \gg 1$). Numerical results were insensitive to the precise value of m. By this policy, $|f_i(s_\alpha)|\,\Delta s_\alpha = |f_i'(s_\alpha)|\,\Delta s_\alpha = O(1/N)$, for all $\alpha = 1, 2, 3, \ldots, 2N$.

The real and imaginary parts of the normal and tangential components of f_i on each meridian-plane contour segment were obtained from the discretized version of (2.7) by solving a dense $8N \times 8N$ linear system that results by explicitly satisfying (the real and imaginary parts of) $u_i = e_i$ at each of the $2N$ collocation points, s_α. Each matrix element was evaluated by numerical integration of (the real and imaginary parts of) S_{ij} on each boundary element, defined by a contour segment and azimuthal rotation, $\Delta s_\alpha \times [0, \pi]$ (evaluation for $[0, -\pi]$ deduced by azimuthal symmetry). A product of one-dimensional adaptive quadrature rules was implemented for this purpose. For unsteady Stokes flow, the surface integrations cannot be analytically reduced to line integrals (Pozrikidis 1989*b*). Diagonal matrix elements that contain the $1/r$ singularity of S_{ij} at $\boldsymbol{x}_0$ were evaluated to relative accuracy $\approx 10^{-4}$; the subdominant, off-diagonal elements were evaluated to an absolute error $\approx 10^{-4}$ times the magnitude of the largest diagonal element. The singular contribution of S_{ij} to the diagonal elements was accurately included by approximating the particle surface at $\boldsymbol{x}_0$ with a small tangent disc of radius a_0 and evaluating the integral on this subinterval analytically (Youngren & Acrivos 1975). For $a_0 \leqslant \Delta s_\alpha/100$, numerical results were insensitive to a_0 for the calculations attempted herein.

A $2N \times 2N$ linear system of equations was obtained from discretizing (2.12) and (2.17). For these equations, each matrix element was evaluated by integrating $Q_i n_i$ on each boundary element, $\Delta s_\alpha \times [-\pi, \pi]$. The azimuthal integrations were performed analytically (Smith & Pierce 1958) and the s-integrations along the contour segments were obtained by one-dimensional adaptive (numerical) quadrature. Diagonal and off-diagonal matrix elements were evaluated to the accuracies described above for the linear system obtained from (2.7). The singular contribution of $Q_i n_i$ to the diagonal elements was accurately included as described for S_{ij} above. In this case, a smaller tangent disc was required, $a_0 = 10^{-4}\Delta s_\alpha$, and the integral of $Q_i n_i$ on this subinterval vanishes. The integral $\int_{S_P} [\nabla_S \cdot \boldsymbol{u}'(\boldsymbol{x})/r]\,\mathrm{d}S(\boldsymbol{x})$ that forms the right-hand-side for the linear system derived from (2.17) was similarly evaluated. First, $\boldsymbol{u}'$ was numerically obtained from (2.12); integration of the $1/r$ singularity was analytically evaluated on a small tangent disc, $a_0 = 10^{-4}\Delta s_\alpha$.

The linear systems derived by discretizing (2.7), (2.12), and (2.17) were solved by

Gaussian elimination. The linear systems associated with (2.12) and (2.17) were diagonally dominant and well-conditioned. At low frequencies, linear systems associated with (2.7) were characteristically ill-conditioned (Karrila & Kim 1989). However, accurate convergent solutions were easily obtained at low frequencies; the estimated condition number decreased significantly for $|\lambda| = O(1)$.

For $|\lambda| \gg 1$, the oscillatory wavelength of S_{ij} (= viscous boundary-layer thickness, $|\lambda|^{-1}$), must be resolved for accurate numerical integration; thus, the number of function evaluations increases as $|\lambda|^2$ for the surface integrations of S_{ij}. The CPU time for solving (2.7) is dominated by numerical integration and, thus, increases as $|\lambda|^2$ at high frequencies. Computations were restricted to $|\lambda| \leqslant 7$, for this reason (Pozrikidis 1989*b*). Thus, we cannot expect to observe the convergence of the fully numerical modified traction, f_i, obtained from (2.7), to the high-frequency form (2.15) obtained from (2.12) and (2.17). However, the results discussed in §4 (figure 2) demonstrate that, away from the cylinder edge, the boundary-layer solution agrees closely with fully numerical calculations even for the modest frequencies considered herein.

Figure 3 reveals that, away from the edge of the cylinder ($|s-1| \geqslant 0.02$), traction profiles obtained with $2N = 40$ contour segments agree very closely with profiles obtained with $2N = 160$ segments. A discretization with 160 segments was used throughout because it gave superior resolution of the traction singularity at $s = 1$. The traction profiles depicted in figures 2(*a*) and 2(*c*) for steady Stokes flow agree with Youngren & Acrivos (1975) to the accuracy of graphical comparison ($\pm 3\%$); unfortunately, no other traction profiles are available for comparison.

After solving for f_i, the unsteady Stokes pressure and velocity at points in the flow interior were obtained by numerical integration of (2.4) and (2.6) using a product of one-dimensional adaptive quadrature rules with 10^{-4} relative error tolerance. After determining Φ on the cylinder surface, the potential flow pressure and velocity were obtained by numerical integration of (2.10); the azimuthal integration was performed analytically, and the s-integration was obtained by adaptive, numerical quadrature (10^{-4} relative error tolerance). Instantaneous streamlines were obtained by integrating the 2×2 system of ordinary differential equations (5.2) using a predictor-corrector algorithm with 10^{-5} relative error tolerance. Contour plots of the pressure field were obtained by interpolation on a rectangular grid with linear spacing $a/100$. Convergence of the velocity and pressure fields obtained by the foregoing procedure was easily obtained.

4. Surface traction

4.1. *Results for smooth particles*

A sphere has particularly simple constant-phase pressure and tangential stress distributions (Stokes 1851):

$$p(\theta) = \tfrac{3}{2}[1+\lambda+\tfrac{1}{3}\lambda^2]\cos\theta, \quad \arg[p(\theta)] = \tan^{-1}\left(\frac{3|\lambda|+\sqrt{2}|\lambda|^2}{3\sqrt{2}+3|\lambda|}\right), \tag{4.1}$$

$$f_\theta(\theta) = \tfrac{3}{2}[1+\lambda]\sin\theta, \quad \arg[f_\theta(\theta)] = \tan^{-1}\left(\frac{|\lambda|}{\sqrt{2}+|\lambda|}\right). \tag{4.2}$$

Recalling the $e^{-i\omega t}$ time dependence, and that locally vanishing tangential stress signals a stagnation point (Batchelor 1967), (4.2) indicates that the local flow field adjacent to the surface apparently stagnates simultaneously over the entire sphere surface

(and subsequently reverses direction) twice in each oscillation cycle: when $\omega t = \cot^{-1}[\arg(f_\theta)]$. Similarly, the pressure on a sphere surface simultaneously vanishes everywhere when $\omega t = \cot^{-1}[\arg(p)]$. The leading-order pressure distribution at high oscillation frequencies, $\frac{1}{2}\lambda^2 \cos\theta$, can be obtained from the potential flow solution; the next term, $\frac{3}{2}\lambda \cos\theta$, can be obtained from the boundary-layer solution according to the procedure described in §2.2.2.

4.2. *Results for a finite-length cylinder*

The pressure and tangential stress distributions on the surface of an axially oscillating cylinder are shown in figures 2 and 3; the normalized magnitude profiles are quantified by the values in table 1. The singularity at $s = 1$ (except for the non-singular potential flow pressure distribution) contrasts markedly with the smooth continuous tractions on a sphere or spheroids (Pozrikidis 1989*b*).

Figure 2(*a*) reveals that $|p(s)|$ is singular at $s = 1$. Figure 2(*b*) shows that $\arg[p(s)]$ has a jump discontinuity of π at $s = 1$ indicating that the pressure distribution changes sign across the edge singularity; this feature persists up to $|\lambda| = 7$, and is evident in the boundary-layer solution. Away from the singular region, $\arg[p(s)]$ tends to $\frac{1}{2}\pi$, the potential flow result, (2.15), that is continuous at $s = 1$. According to figure 2(*b*), the pressure vanishes on points that originate from the symmetry axis ($s = \pm 2$) and travel towards the centreline ($s = 0$).

Figure 2(*c*) indicates that the tangential stress distribution is also singular at $s = 1$. By the argument beneath (4.2), the results shown in figure 2(*d*) imply that two stagnation points, s_0^* and s_2^* (the subscript denotes the initial location: $s = 0$ and $s = 2$), appear on the side and face of the cylinder surface during decelerating portions of the oscillation cycle. The first stagnation point to appear, s_2^*, emanates from the symmetry axis ($s = 2$) and travels along the cylinder surface to the edge at $s = 1$; s_0^* emanates from the centreline ($s = 0$) slightly later in the cycle, and also travels to the edge. Apparently, flow reversal occurs last at the edge of the cylinder. By fore-aft symmetry, additional stagnation points, $-s_0^*$ and $-s_2^*$, travel simultaneously towards the rear edge at $s = -1$. Stagnation points (and $p = 0$ points) travel slowest near the cylinder edge. This four-stagnation-point flow reversal process on a cylinder surface is more complex than the reversal processes for a sphere (no travelling stagnation points) or spheroids (two stagnation points) (Pozrikidis 1989*b*).

Figure 2(*d*) and (4.2) indicate that flow reversal begins on the face and side of the cylinder surface before simultaneous flow reversal occurs on a sphere (oscillating at the same frequency). At lower frequencies ($|\lambda| \leqslant 1$), complete surface flow reversal occurs at essentially the same time in the cycle for a cylinder and a sphere; however, complete surface flow reversal for a cylinder is relatively delayed at higher frequencies ($|\lambda| = 3$ and 7). In the limit $|\lambda| \to \infty$ the boundary-layer solution, (2.16), indicates that simultaneous flow reversal occurs everywhere on any particle surface when $\omega t = \frac{1}{4}\pi$. Figure 2(*d*) reveals that $\arg[f_s(s)] > \frac{1}{4}\pi$ on the face of the cylinder ($1 \leqslant s \leqslant 2$) for intermediate frequencies and is maximal for $|\lambda| \approx 3$; this feature was also observed for spheroids (Pozrikidis 1989*b*).

The boundary-layer solution is only valid for $|\lambda| \gg 1$ and away from the cylinder edge: $|s-1| \gg |\lambda|^{-1}$. The potential flow and boundary-layer solutions depicted in figure 2 are evaluated with $|\lambda| = 7$ and the magnitude profiles are normalized consistently with fully numerical results for $|\lambda| = 7$; a direct comparison is thus possible. In the region of validity, figure 2 and table 1 indicate that the boundary-layer solution accurately approximates fully numerical calculations even at the modest frequency $|\lambda| = 7$. According to the results depicted in figure 2, the boundary-layer solution is

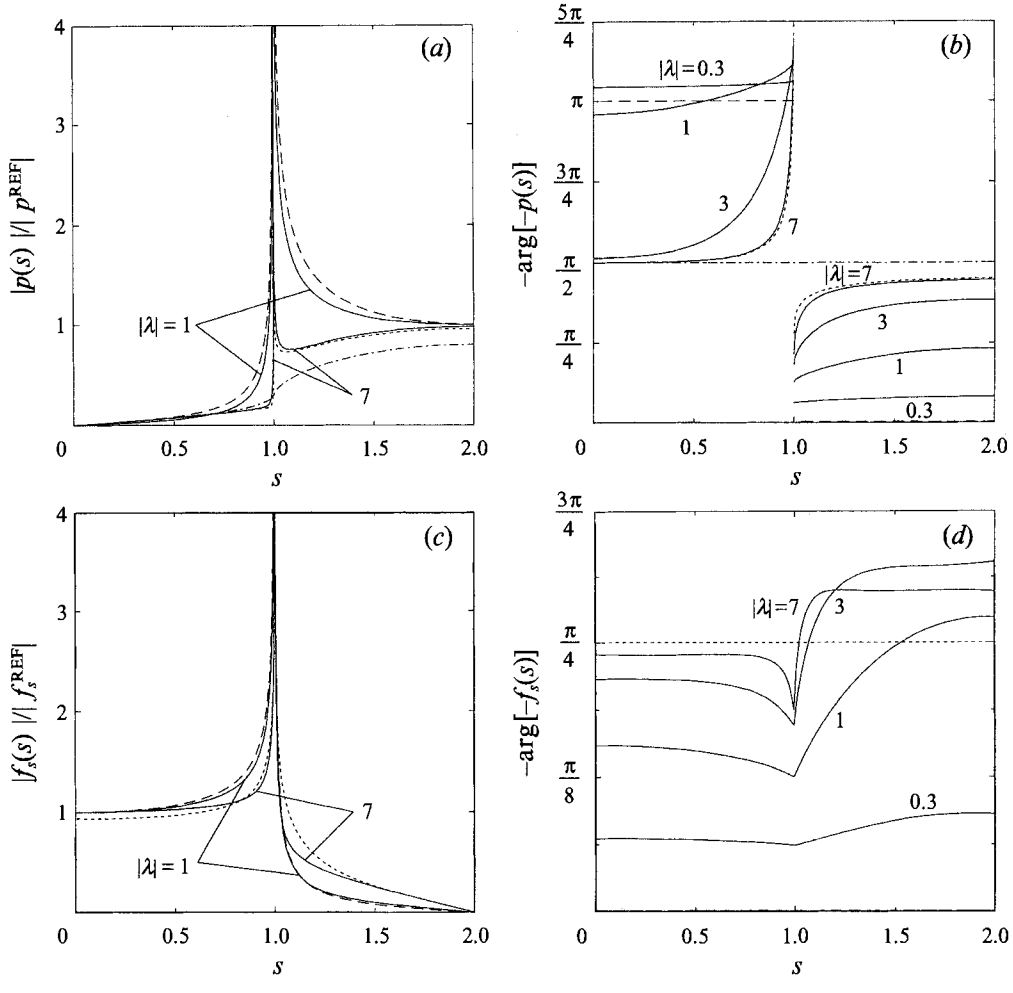

FIGURE 2. Magnitude and phase of normalized pressure (*a*, *b*), and tangential stress (*c*, *d*), distributions. Solid curves: results for $|\lambda|$ as labelled; dashed curves: $|\lambda| = 0$ results; dashed-dotted curves: potential-flow pressure; dotted curves: boundary-layer solution (with $|\lambda| = 7$). Numerical values for $|p^{REF}|$ and $|f_s^{REF}|$ supplied in table 1. For $|\lambda| = 0$ and 1, $|p^{REF}| = |p(2)|$. For $|\lambda| = 7$, potential flow, and boundary-layer solution, $|p^{REF}| = |\lambda|^2 = 49$ (for comparison). For $|\lambda| = 0$, 1 and 7, $|f_s^{REF}| = |f_s(0)|$; for boundary-layer solution, $|f_s^{REF}| = |f_s(0)|$ with $|\lambda| = 7$ (= 8.49) (for comparison).

	$\|\lambda\| = 0$	$\|\lambda\| = 0.3$	$\|\lambda\| = 1$	$\|\lambda\| = 3$	$\|\lambda\| = 5$	$\|\lambda\| = 7$
$\|p(2)\|$	1.05 (—)	1.37 (—)	2.61 (22%)	11.0 (6%)	25.6 (4%)	47.0 (4%)
$\|f_s(0)\|$	0.754 (—)	0.969 (—)	1.61 (30%)	3.83 (11%)	6.10 (7%)	8.49 (7%)

TABLE 1. Numerical values used to normalize pressure and tangential stress magnitude profiles in figure 2, except as noted in figure caption 2. Also shown is the percentage error (relative to fully numerical calculations) of the boundary-layer solution: $p(2) = 0.765\lambda^2 + 1.43\lambda$, $f_s(0) = 1.13\lambda$.

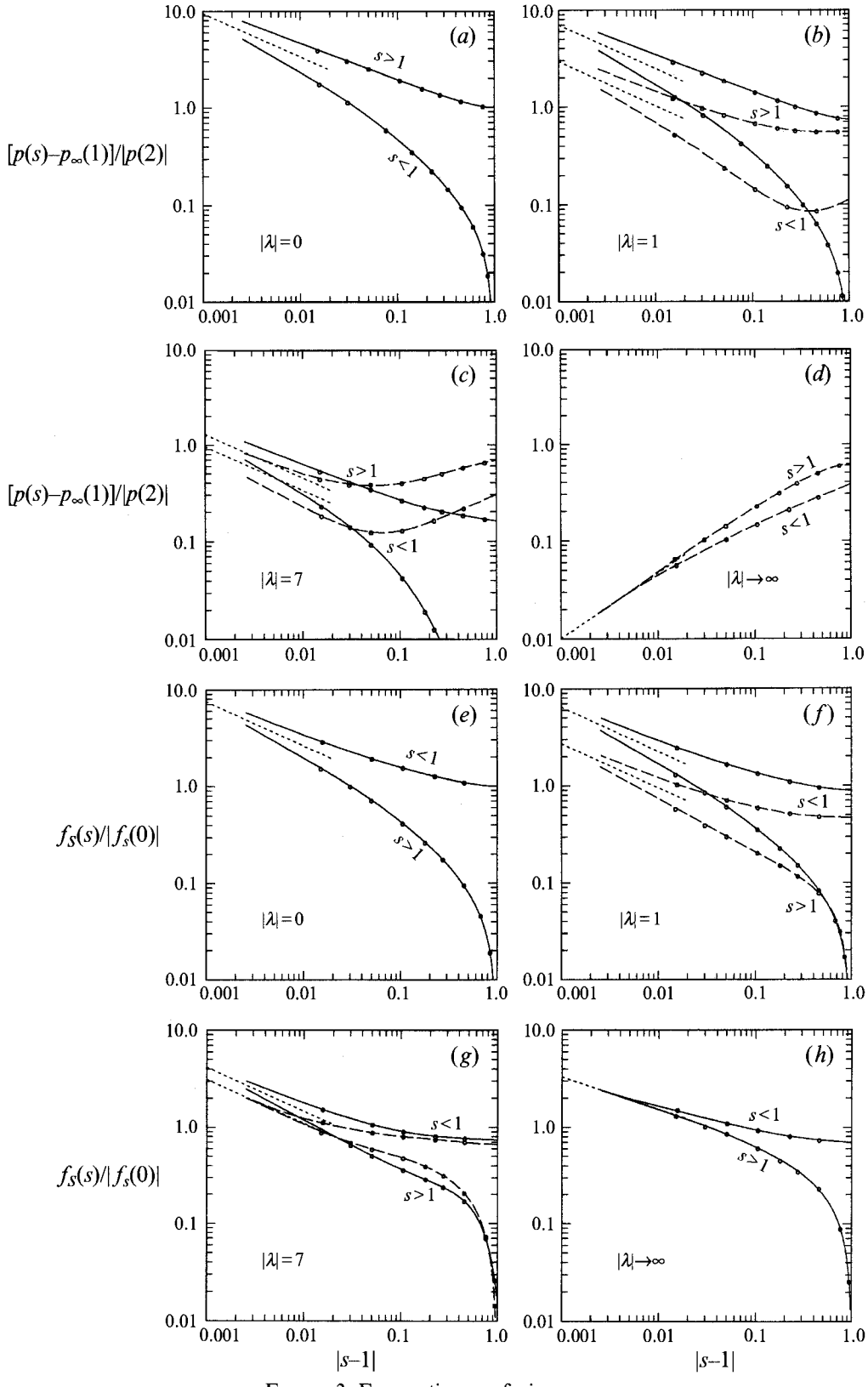

FIGURE 3. For caption see facing page.

most accurate along the cylinder side ($|s| \leqslant 1$), suggesting that the boundary layer is thinner there.

For two-dimensional viscous flow around a 90° corner, Dean & Montagnon (1949) showed that near the corner ($s \to 1$), the pressure and tangential stress distributions are singular: $p(s) \sim \text{sign}\,(s-1)\,|s-1|^{-0.455516\cdots}$ and $f_s(s) \sim |s-1|^{-0.455516\cdots}$. A simple, local analysis (Jackson 1962) reveals that $[\Phi(s)-\Phi(1)] \sim |s-1|^{\frac{2}{3}}$ for potential flow around a 90° corner. It follows that near the corner, $[p(s)-\lambda^2\Phi(1)] \sim \lambda^2|s-1|^{\frac{2}{3}}$ for potential flow, and $f_s'(s) \sim |s-1|^{-\frac{1}{3}}$ for the boundary-layer flow. A similar local analysis of (2.14*c*) reveals that the boundary-layer solution for the excess pressure is singular at the cylinder edges: $p(s)' \sim \text{sign}\,(s-1)\,|s-1|^{-\frac{1}{3}}$. Apparently, the two-dimensional pressure and tangential stress distributions are equally singular at $s = 1$ in the low- and high-frequency limits; the pressure has a discontinuous sign change and the tangential stress has constant sign across the singularity. However, the singularity is stronger in the low-frequency limit ($-0.455516\ldots$ versus $-\frac{1}{3}$), and the high-frequency pressure distribution is continuous at leading order. These two-dimensional flow analyses qualitatively explain the singular tractions observed in figure 2.

The results depicted in figure 3 suggest that the steady two-dimensional viscous flow singularity persists at the cylinder edge for finite $|\lambda|$. Near the cylinder edge, an appropriate characteristic length for the local flow field is $|s-1|\,a$, not the particle dimension, a. Thus, a modified frequency parameter, $\lambda|s-1|$, describes the unsteady character of the flow field near $s = 1$. For $|s-1| \ll 1$, the local flow field is two-dimensional. Accordingly, singular, two-dimensional, steady Stokes flow characterizes the region $|s-1|\,(1+|\lambda|) \ll 1$. This claim explains the confinement of manifest singular pressure to a smaller region near $s = 1$ with increased $|\lambda|$ because $p(s)$ is continuous to leading order for $|\lambda| \gg 1$ (figures 2*a*, *b*, 3 *a–d*). The tangential stress is singular in both limiting regimes so a singularity confinement is not observed in figures 2(*c*, *d*) and 3(*e–h*). The existence of a two-dimensional steady Stokes region also explains the pronounced phase angle minima for the tangential stress distributions at finite $|\lambda|$ observed in figure 2(*d*); the local phase shift at $s = 1$ is non-vanishing because the local flow field interacts with the unsteady flow field away from the cylinder edge.

The boundary-layer solution varies rapidly in the region $|\lambda|^{-1} \ll |s-1| \ll 1$, ($|\lambda| \gg 1$); the two-dimensional analysis predicts $1 \ll |f_s'(s)| \ll |\lambda|^{\frac{1}{3}}$, but the pressure is constant to leading order, $p(s) = \lambda^2\Phi(1) + O(|\lambda|^{\frac{4}{3}})$. Unfortunately, this prediction cannot be observed because the region $|\lambda|^{-1} \ll |s-1| \ll 1$ is non-existent for the moderate frequencies considered herein ($|\lambda| \leqslant 7$). the boundary-layer solution breaks down for $|s-1| = O(|\lambda|^{-1})$ because the boundary layer is not thin compared to the characteristic (tangential) lengthscale. Thus, a two-dimensional boundary-layer singularity cannot occur; the regions near $s = \pm 1$ that are described by a two-dimensional steady Stokes singularity and a two-dimensional boundary-layer solution are non-overlapping.

FIGURE 3. Normalized absolute values of real (solid curves) and imaginary (dashed curves) components of pressure (*a–d*), and tangential stress (*e–h*), distributions; curves: $2N = 160$, circles: $2N = 40$ contour segments. Profiles for $0 \leqslant s \leqslant 1$ and $1 \leqslant s \leqslant 2$ as labelled. Dotted curves: singular behaviour for steady two-dimensional viscous (*a–c*, *e–g*), potential (*d*), and boundary-layer (*h*) flows. Note: $p_\infty(1) = 0.294\lambda^2$ (potential flow). See table 1 for $|p(2)|$ and $|f_s(0)|$ values.

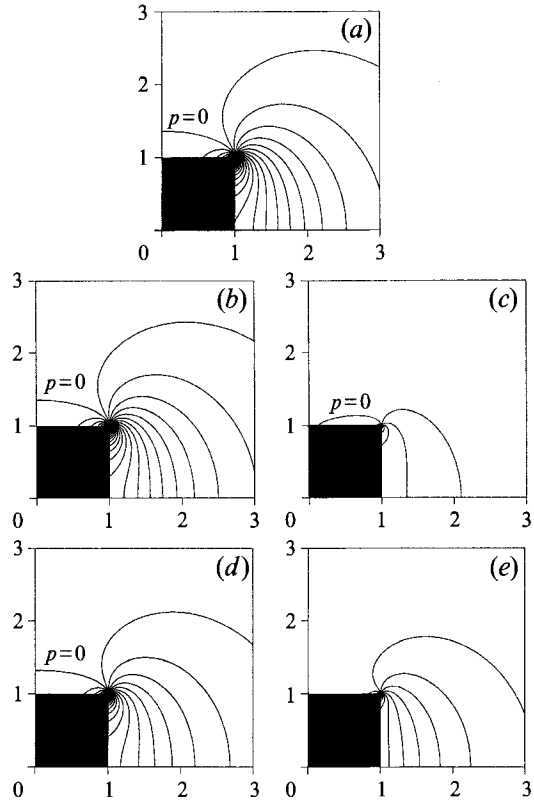

FIGURE 4. For caption see facing page.

5. Flow field

5.1. *Pressure field*

The pressure field, $p(\boldsymbol{x})$, is axisymmetric and fore-aft antisymmetric. By (2.6), $p(\boldsymbol{x})$ depends only on the instantaneous pressure distribution on the particle surface and tends to a dipole in the far-field:

$$p(\boldsymbol{x}) = \tfrac{1}{2}e_i[R_{ij} + \lambda^2 V_P \delta_{ij}]\, Q_j, \quad r \gg 1, \tag{5.1}$$

for oscillating particles of any shape. According to (2.8) and (2.18), the pressure is in phase with the particle velocity at low frequencies, and in phase with the particle acceleration at high frequencies.

The pressure field produced by an oscillating sphere is a simple dipole everywhere (Stokes 1851): $p(\boldsymbol{x}) = p(\theta)/r^2$, where $p(\theta)$ is the surface pressure distribution, (4.1). This simple, smoothly varying field contrasts with the near-field pressure for an axially oscillating cylinder depicted in figure 4. The real-valued steady Stokes pressure field, shown in figure 4(*a*), is qualitatively distinct from the imaginary-valued potential flow pressure field in figure 4(*j*). The steady Stokes pressure field exhibits large pressure gradients near the edge of the cylinder and a region of suction ($p < 0$) along the side of the cylinder that is bounded by the labelled $p = 0$ isobar. By contrast, the potential flow pressure field has only modest pressure gradients near the edge of the cylinder and has the same sign everywhere forward of the centreline. The pressure fields for finite oscillation frequencies are complex-valued. The tendency of the pressure field to the

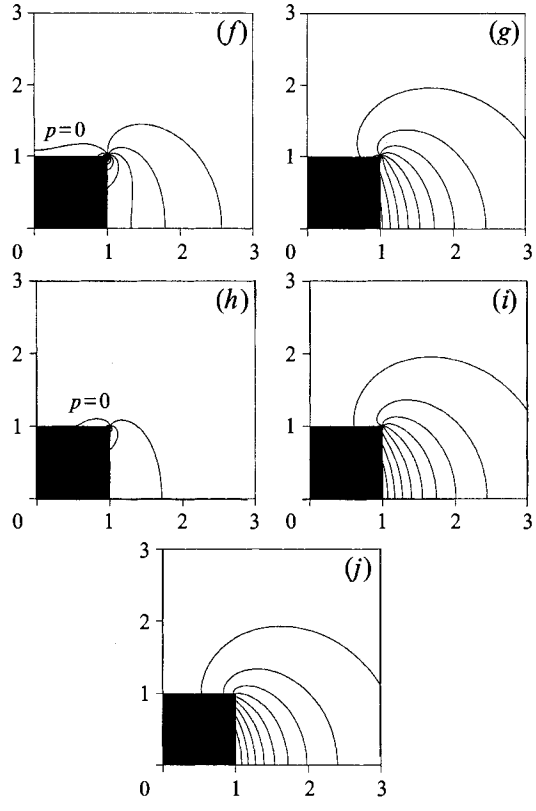

FIGURE 4. Pressure fields: real-valued field for $|\lambda| \to 0$ (*a*); real and imaginary fields (*b*, *c*), (d, *e*), (*f*, *g*), (*h*, *i*) for $|\lambda| = 0.3, 1, 3, 7$; imaginary-valued field for $|\lambda| \to \infty$ (*j*). By symmetry, only a side view of the upper half of the cylinder and surrounding pressure field are shown. Isobars separated by $|p(2)|/10$ ($p(2)$ given in table 1).

far-field dipole form (5.1), and the transition from the real-valued steady Stokes pressure field to the imaginary-valued potential flow field with increasing $|\lambda|$, are apparent in figure 4.

5.2. *Velocity field*

Pathlines coincide with streamline segments whenever $\boldsymbol{u}(\boldsymbol{x})$ has constant phase or is quasi-steady; this is true for $|\lambda| r \ll 1$ and $|\lambda| r \gg 1$. In general, however, (instantaneous) streamlines differ from pathlines in oscillatory Stokes flow: streamlines show kinematical features of the velocity field, and pathlines convey the net convective properties.

5.2.1. *Instantaneous streamlines*

Streamlines (tangent to the instantaneous velocity field) at a particular instant in the oscillation cycle, $\omega t = \tau_0$, are described by

$$\frac{\mathrm{d}x}{\mathrm{Re}\{u(x,y)\,\mathrm{e}^{-\mathrm{i}\tau_0}\}} = \frac{\mathrm{d}y}{\mathrm{Re}\{v(x,y)\,\mathrm{e}^{-\mathrm{i}\tau_0}\}}, \tag{5.2}$$

where (x, y) are Cartesian coordinates in a meridian plane: x parallel and y normal to the symmetry axis; u and v are the corresponding velocity components relative to the

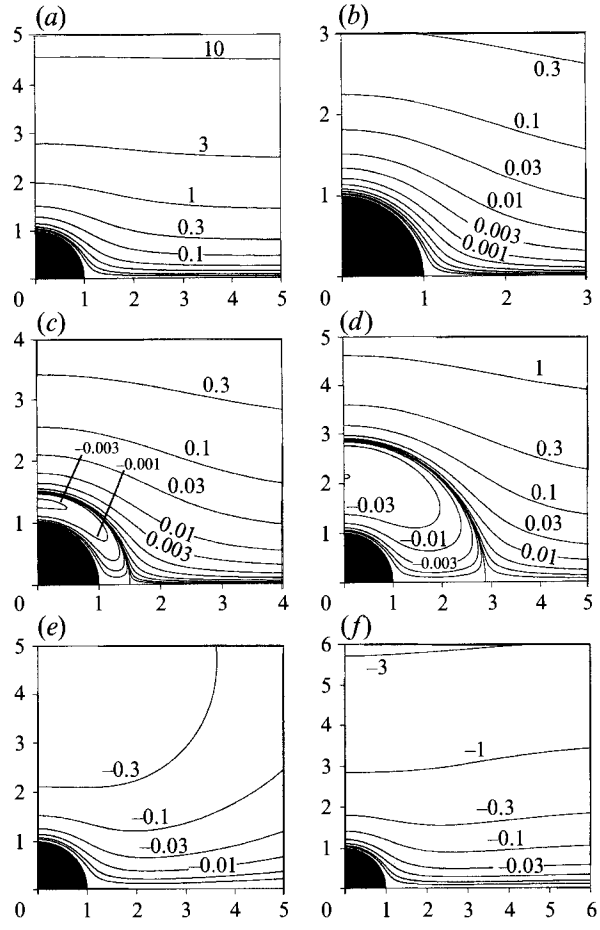

FIGURE 5. Instantaneous streamlines for oscillating sphere, $|\lambda| = 1$. Stream-function values follow the sequence: $\psi = 10, 3, 1, 0.3, 0.1, \ldots, 0, \ldots, -0.1, -0.3, -1, -3$. Note: length scale changes in each part of the figure as indicated. (*a*) $\omega t = 0$; (*b*) 0.375π; (*c*) 0.40π; (*d*) 0.45π; (*e*) 0.50π; (*f*) 0.55π.

particle. Initial conditions are obtained from selected values of the Stokes stream function (Kim & Karrila 1991):

$$\psi(x_0, y_0) = \int_{(x_0,0)}^{(x_0,y_0)} \mathrm{Re}\{u(x_0, y)\, \mathrm{e}^{-\mathrm{i}\tau_0}\}\, y \, \mathrm{d}y.$$

Sphere. In figure 5, a sequence of instantaneous streamline patterns depicts the unsteady flow past an oscillating sphere with $|\lambda| = 1$; the streamlines are shown in the (accelerating) reference frame of the particle. According to (4.2), surface flow reversal (simultaneously) occurs when $\omega t = \frac{3}{8}\pi$ ($|\lambda| = 1$); at this instant, the streaming flow pattern is very weak as stream-function values in figure 5(*b*) indicate. Immediately thereafter, a thin region of reversed flow envelopes the entire sphere surface; an eddy in the shape of a thin spherical shell is formed that is associated with two stagnation points travelling away from the sphere surface along the symmetry axis. As the sphere decelerates further, figure 5(*c*, *d*) shows that stagnation points travel further outward and the spherical-shell eddy expands: vorticity diffuses away from the sphere surface; the recirculating eddy has a radius of 2.88 when $\omega t = 0.45\pi$. Increasingly negative stream-function values within the expanding eddy reflect the growing reverse-flow

strength. The eddy expands to infinity for $\omega t \to \frac{1}{2}\pi$, as discussed below, terminating the near-field flow reversal process.

Finite-length cylinder. According to figure 2(*d*), axisymmetric near-field flow reversal for the finite-length cylinder with $|\lambda| = 1$ begins when $\omega t \approx 0.23\pi$ as two stagnation points emanate from the symmetry axis and travel along the cylinder faces towards the edges; two additional stagnation points simultaneously travel away from the cylinder along the symmetry axis. Thus, two toroidal eddies are formed that are attached to the front and rear cylinder faces and wrap around the symmetry axis (figure 6*b*), similar to the near-field flow reversal past an oblate spheroid (Pozrikidis 1989*b*). The fore-aft eddies expand gradually during the interval $0.23\pi \leqslant \omega t \leqslant 0.35\pi$ covering the cylinder faces ($1.1 \leqslant |s| \leqslant 2$); stream-function values reveal a weak recirculating flow. Figure 2(*d*) indicates that two additional stagnation points emanate from the cylinder centreline when $\omega t \approx 0.35\pi$ and travel along the surface towards the edges. This signals the birth of a third toroidal eddy that wraps around the cylinder centreline (figure 6*c*), similar to the single eddy that forms during near-field flow reversal past a prolate spheroid (Pozrikidis 1989*b*); stream-function values indicate that the recirculating flow is comparable in all eddies.

As the cylinder decelerates further, figure 6(*d–f*) shows that the side eddy quickly expands and gathers strength, dominating the recirculating flow in the fore-aft eddies. According to figure 2(*d*), eddy coalescence occurs as the four travelling stagnation points reach the cylinder edges, $s = \pm 1$, when $\omega t \approx \frac{3}{8}\pi$ (figure 6*d–f*). A single eddy results after coalescence that envelopes the entire cylinder. Its evolution and the remainder of the near-field flow reversal process (figure 6*g–i*), is qualitatively the same as for a sphere; the single eddy is slightly elongated and has a somewhat larger mean radius: 3.30 when $\omega t = 0.45\pi$.

General features. Simple, streaming flow, corresponding to the real component of the velocity field, is observed when the particle velocity is maximal ($\omega t = 0$); the same qualitative streamline pattern occurs during the accelerating, and first part of the decelerating, portions of the oscillation cycle. $\mathrm{Re}\{\boldsymbol{u}(\boldsymbol{x})\}$ is qualitatively described by steady Stokes flow near the particle surface ($|\lambda| r \ll 1$), and by potential flow far from the particle ($|\lambda| r \gg 1$) (cf. figures 5*a* and 6*a*). Streamlines (= pathlines) for steady Stokes and potential flow are depicted in figure 7(*a*, *c*) for a sphere and in figure 7(*b*, *d*) for a cylinder. These velocity fields are quasi-steady: for an oscillating particle, the stream function varies as $\cos \omega t$ with amplitudes given by the values in the figure caption. The qualitative similarity between the simple streaming flow patterns depicted in figures 5(*a*), 7(*a*), and 7(*c*), and those depicted in figures 6(*a*), 7(*b*), and 7(*d*) indicates that detailed particle geometry is unimportant for the quasi-steady flows, or the real part of the unsteady velocity field.

As the oscillation cycle progresses, the particle and surrounding flow field decelerate but the streaming flow pattern persists; it is interrupted after further deceleration by an unsteady near-field flow reversal process, initiated by surface flow reversal. Surface flow reversal is affected by the detailed particle geometry (cf. §4), thus it follows that the initial stages of unsteady near-field flow reversal are sensitive to particle shape. As explained beneath (5.4), the flow field is everywhere reversed and the particle stationary when $\omega t = \frac{1}{2}\pi$. The streaming flow pattern is immediately resumed for $\pi > \omega t > \frac{1}{2}\pi$ (e.g. figures 5*e*, *f* and 6*i*, *j*). The foregoing unsteady flow reversal process repeats exactly a half-cycle later during third-quarter deceleration.

The instantaneous streamline patterns for different frequency parameters are qualitatively the same as those depicted in figures 5 and 6 for $|\lambda| = 1$. The unsteady flow reversal process has the most overall significance for $|\lambda| \approx 1$. The recirculating eddy

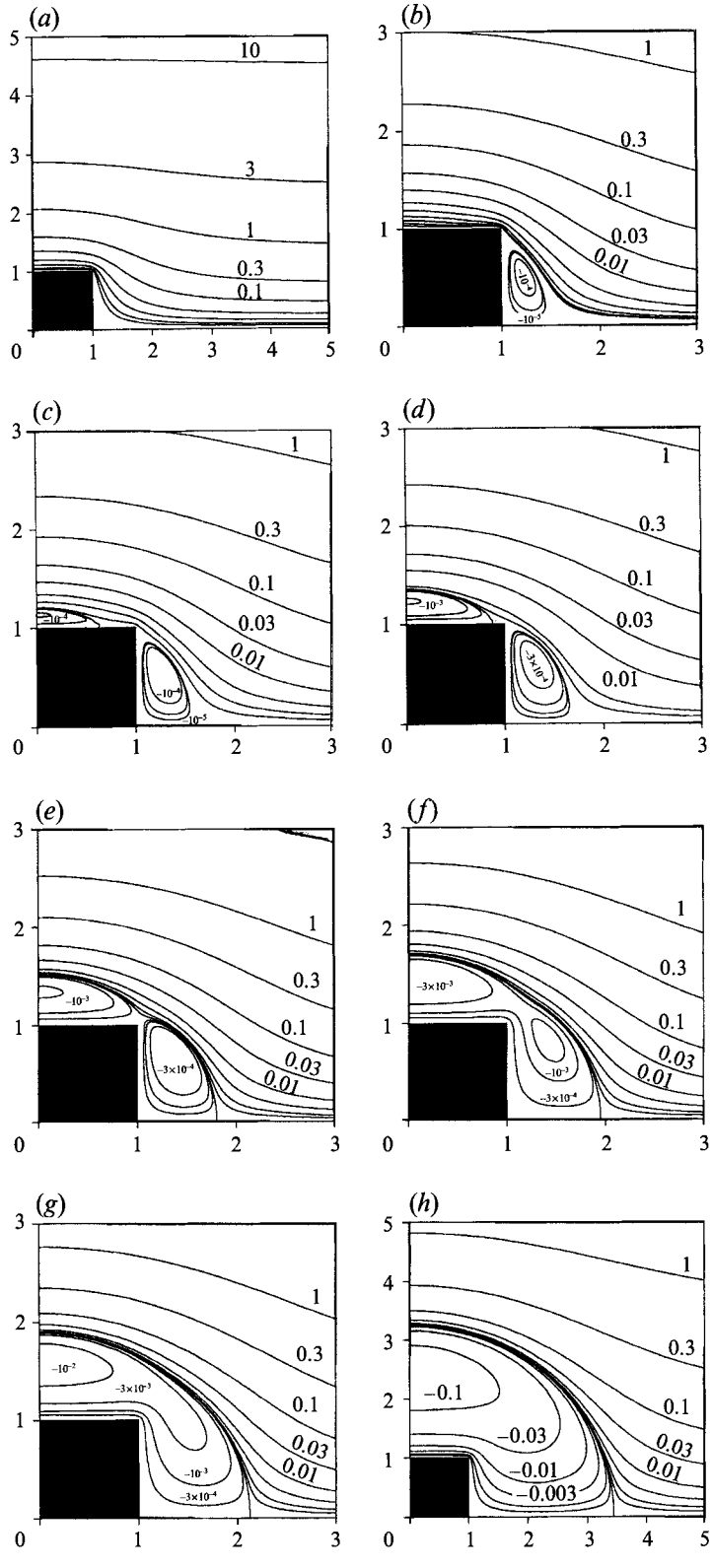

FIGURE 6 (*a–h*). For caption see facing page.

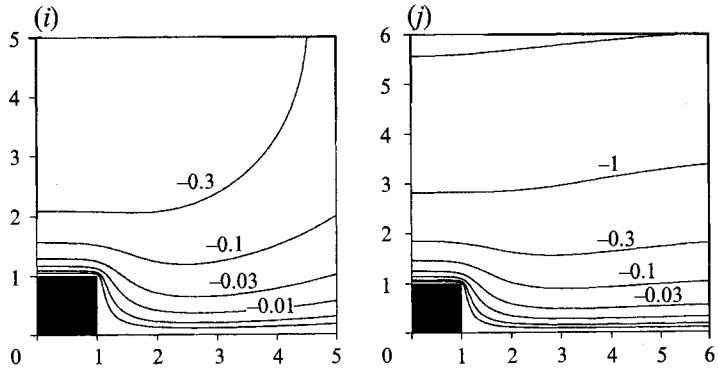

FIGURE 6. Instantaneous streamlines for oscillating cylinder $|\lambda| = 1$. Stream-function values follow the sequence: $\psi = 10, 3, 1, 0.3, 0.1, \ldots, 0, \ldots, -0.1, -0.3, -1, -3$. Note: it was not possible to determine the $\psi = 0$ streamlines in (*b–d*); the length scale changes in each part of the figure, as indicated. (*a*) $\omega t = 0$, (*b*) 0.35π; (*c*) 0.36π; (*d*) 0.37π; (*e*) 0.38π; (*f*) 0.39π; (*g*) 0.40π; (*h*) 0.45π; (*i*) 0.50π; (*j*) 0.55π.

forms earlier in the cycle at higher oscillation frequencies but is compressed closer to the particle surface; for $|\lambda| \gg 1$, the recirculating eddy generally lies within a thin $O(|\lambda|^{-1})$ boundary layer (except when $\omega t \to \frac{1}{2}\pi$ and $\frac{3}{2}\pi$ as discussed below). After the recirculating eddy envelops an oscillating particle and assumes a nearly spherical shape, its radius is given by the location of the stagnation points that move outward from the particle surface (cf. figures 5*c*, *d* and 6*e–h*). Eddy expansion is depicted in figure 8 by the location of stagnation points for the case of a sphere or a cylinder with $|\lambda| = 0.3, 1, 3, 7$.

Far from an arbitrary-shaped particle, the size and evolution of the unsteady viscous flow reversal eddy can be predicted by examining the far-field stream function derived from (5.1) with the help of (2.11):

$$\psi = \tfrac{1}{2}r^2 \sin^2\theta \mathrm{Re}\left\{\left[\frac{e_i e_j R_{ij} + \lambda^2 V_P}{2\pi\lambda^2 r^3} - 1\right] e^{-i\omega t}\right\}, \quad r \gg 1 + |\lambda|^{-1}, \tag{5.3}$$

which has constant phase: $\arg[R_{ij} + \lambda^2 V_P \delta_{ij}] + \frac{1}{2}\pi$. The result indicates that the eddy becomes spherical as it expands; its outer radius is obtained by solving for $\mathrm{Re}\{\psi\} = 0$:

$$r = \left[\frac{e_i e_j \mathrm{Re}\{R_{ij}\}}{2\pi|\lambda|^2\delta}\right]^{\frac{1}{3}}, \quad \delta \to 0, \tag{5.4}$$

where $\delta = \frac{1}{2}\pi - \omega t$ or $\frac{3}{2}\pi - \omega t$. The $\delta^{-\frac{1}{3}}$ singular behaviour for $\omega t \to \frac{1}{2}\pi$, and the weak, $[\mathrm{Re}\{R_{ij}\}]^{\frac{1}{3}}$, shape dependence are illustrated in figure 8 for the case of a sphere and a cylinder. According to (5.3) and (5.4), the (tangential) velocity on the eddy surface is $\frac{3}{2}\delta \sin\theta$, *independent* of particle shape and oscillation frequency: the eddy vanishes, and the flow is everywhere reversed for $\delta \to 0$. For $|\lambda| = 1$ and $\omega t = 0.45\pi$, the asymptotic formula, (5.4), yields $r = 3.19$ and $r = 3.50$ for a sphere and cylinder, fairly close to the numerical results quoted above, even for the moderately large value $\delta = \pi/20$. At the same frequency and phase, the formula predicts $r = 4.23$ and $r = 2.99$ for a prolate and oblate spheroid, in reasonable agreement with numerical values, $r = 4.5$ and $r = 2.6$ obtained from Pozrikidis (1989*b*).

The recirculating eddy is an unsteady viscous effect that is manifested in the irrotational far-field; it is a long-range effect, albeit short-lived. Viscous effects are

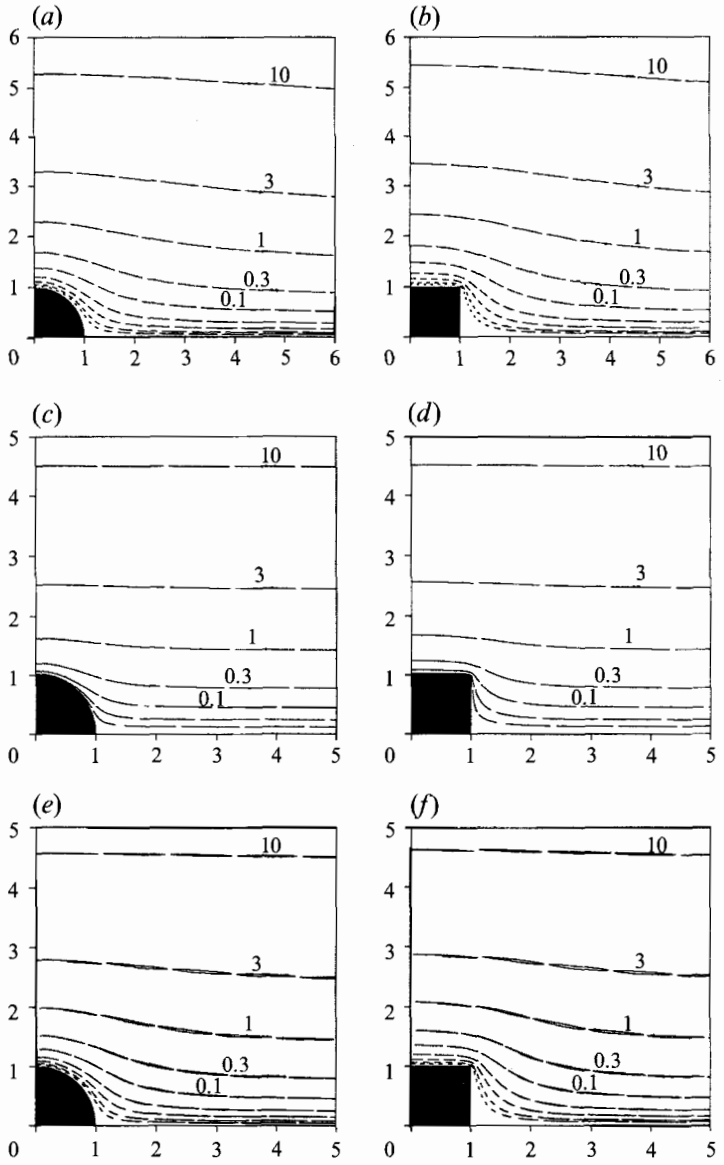

FIGURE 7. Pathlines (and streamlines) for flow past a sphere and cylinder; $Sl = 2$: $\lambda = 0$ (a,b); $|\lambda| \to \infty$ (c,d); $|\lambda| = 1$ (e,f). Initial points on $\omega t = 0$ streamlines corresponding to $\psi = 10, 3, 1, \ldots$. Note the length scale in each part of the figure.

directly responsible for the near-field reversal process, and the latter determines kinematical features of the entire flow reversal process, even for $|\lambda| r \gg 1$. For an arbitrary particle, the low- and high-frequency formulae are obtained from (2.8) and (2.18): $\mathrm{Re}\{R_{ij}\} = R^0_{ij} + |\lambda| R^0_{ik} R^0_{kj}/6\sqrt{2}\pi$ and $\mathrm{Re}\{R_{ij}\} = |\lambda| B^\infty_{ij}/\sqrt{2}$ for $|\lambda| \ll 1$ and $|\lambda| \gg 1$. Thus, according to (5.4), the eddy radius (for fixed ωt) is $O(|\lambda|^{-\frac{2}{3}})$ at low frequencies and $O(|\lambda|^{-\frac{1}{3}})$ at high frequencies for $\delta \to 0$, in contrast to the $O(|\lambda|^{-1})$ eddy radius predicted for earlier stages of its evolution, $\delta = O(1)$.

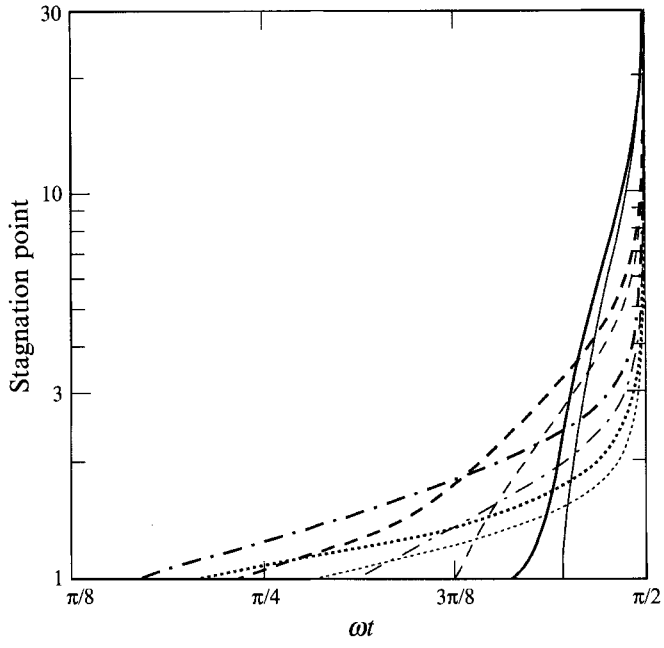

FIGURE 8. Instantaneous location of stagnation point along symmetry axis of an oscillating cylinder (thicker curves) and sphere (thinner curves) as a function of phase during the oscillation cycle. ——, $|\lambda| = 0.3$; – –, $|\lambda| = 1$; – · –, $|\lambda| = 3$; ·····, $|\lambda| = 7$.

5.2.2. *Pathlines*

The (axisymmetric) trajectories of fluid elements during one oscillation cycle (pathlines) are described by

$$Sl\frac{\mathrm{d}x}{\mathrm{d}\tau} = \mathrm{Re}\{u(x,y)\,\mathrm{e}^{-\mathrm{i}\tau}\}, \quad Sl\frac{\mathrm{d}y}{\mathrm{d}\tau} = \mathrm{Re}\{v(x,y)\,\mathrm{e}^{-\mathrm{i}\tau}\}, \tag{5.5}$$

$$0 \leqslant \tau \leqslant 2\pi; \quad \tau = 0: \quad x,y = x_0,y_0,$$

where (x,y) and (u,v) are defined beneath (5.2), and $\tau = \omega t$. By the assumption of small-amplitude oscillations, $Sl \gg |\lambda|^2, \boldsymbol{u}(\boldsymbol{x}) \approx \boldsymbol{u}(\boldsymbol{x}_0)$; thus, (5.5) is integrated to yield

$$Sl(\boldsymbol{x}-\boldsymbol{x}_0) = \mathrm{Re}\{\boldsymbol{u}(\boldsymbol{x}_0)\}\sin\tau - \mathrm{Im}\{\boldsymbol{u}(\boldsymbol{x}_0)\}(1-\cos\tau), \quad 0 \leqslant \tau \leqslant 2\pi, \tag{5.6}$$

indicating that pathlines for linearized oscillatory flows are closed elliptical orbits, linear in Sl. Pathlines for steady Stokes flow, potential flow, and unsteady Stokes ($|\lambda| = 1$) are depicted in figure 7. Since pathlines are linear in Sl, $Sl = 2$ was used to help visualize pathline structure; however, pathlines would generally be much smaller than those depicted in figure 7 because $Sl \gg 1$.

Unsteady Stokes pathlines (figure 7*e*, *f*) and streamlines for the real component of the velocity field (figures 5*a* and 6*a*) agree closely. Apparently, $\mathrm{Re}\{\boldsymbol{u}(\boldsymbol{x})\}$ dominates convective processes in linearized low-Reynolds-number flows, thus (5.6) reduces to

$$Sl(\boldsymbol{x}-\boldsymbol{x}_0) \approx \mathrm{Re}\{\boldsymbol{u}(\boldsymbol{x}_0)\}\,t, \quad -1 \leqslant t \leqslant 1. \tag{5.7}$$

Since $\mathrm{Re}\{\boldsymbol{u}(\boldsymbol{x})\}$ is insensitive to the detailed particle geometry, we conclude the same for the pathlines of oscillatory Stokes flow.

On the assumption that fluid displacement is $O(a/Sl)$, it follows that the effect of small-amplitude oscillatory motion is qualitatively similar to an anisotropic diffusivity,

$D/\nu = O(Re/Sl)$, tangent to the surface of an oscillating particle. Thus, for linearized oscillatory flow, convection is unlikely to significantly facilitate mass transport. Convective enhancement by oscillatory flow generally requires the steady-streaming flow associated with finite Reynolds numbers (e.g. Ghaddar *et al.* 1986).

6. Concluding remarks

The flow field generated by axial oscillations of a finite-length cylinder in a viscous liquid under low-Reynolds-number conditions has been examined in detail. Numerical calculations were performed using a first-kind boundary integral formulation. A boundary-layer solution that involves two frequency-independent second-kind boundary integral equations was formulated for high oscillation frequencies. Numerical results were obtained by discretizing the integral equation and approximating the traction by a piecewise-continuous function. An unequal discretization policy was implemented, based on the predicted traction singularities at the cylinder edge. Boundary integral calculations were successful for moderate oscillation frequencies ($|\lambda| \leqslant 7$); when successful, the boundary integral calculations appear to be pointwise valid and capable of probing the singular behaviour at non-smooth boundaries. Convergence was obtained with $2N = 40$ boundary elements but 160 elements were used because this gave superior resolution of the traction singularities at the cylinder edge. The second-kind integral equations for the boundary-layer solution were solved by a similar procedure. Away from the singular region near the cylinder edge, the boundary-layer solution agrees closely with fully numerical calculations even for the modest frequency parameter $|\lambda| = 7$.

Traction distributions for unsteady Stokes flow are singular for all oscillation frequencies at the cylinder edge ($|s-1| \ll 1$) and characterized by two-dimensional flow around a 90° corner. A local two-dimensional analysis qualitatively predicts the singular behaviour. For $|s-1| \ll (1+|\lambda|)^{-1}$, a two-dimensional steady Stokes flow singularity is predicted and several qualitative features were observed. We should note that a mathematically exact particle edge or corner is an unrealistic surface feature: the local radius of curvature has a physical lower bound, ≈ 1 nm, dictated by the breakdown of the continuum approximation, implicit in (1.1); thus, $|s-1| \geqslant 1/1000$ for a micron sized particle. The results depicted in figure 3, indicate that large tractions can, nevertheless, occur at sharp physical surface features.

The pressure field is complex-valued; the real component of the near-field pressure resembles the rapidly varying steady Stokes pressure field and the imaginary component resembles the smoother potential flow field. Instantaneous streamline plots for $|\lambda| = 1$ reveal complex kinematical features of the axisymmetric oscillatory flow field past a cylinder. Three toroidal eddies form during the decelerating portions of the oscillation cycle that are attached to the cylinder surface at the travelling stagnation points: one eddy on each of the flat faces of the cylinder and a third that wraps around the centreline. The eddies grow and coalesce as the stagnation points reach the edges, forming a single eddy that encloses the entire particle. Initiation of this near-field flow reversal process is consistent with tangential stress profiles that reveal four stagnation points on the cylinder surface, two emanating from the symmetry axis and two from the cylinder centreline, all travelling towards the edges of the cylinder where reversal occurs last. This contrasts with simpler processes for a sphere or spheroid; it is sensitive to particle geometry. However, most of the oscillatory flow cycle is similar for all particles: the recirculating eddy expands and vanishes when the particle changes direction, a simple streaming flow pattern, associated with $\mathrm{Re}\{\boldsymbol{u}(\boldsymbol{x})\}$ and insensitive to

particle shape, persists during the remainder of the flow cycle. Pathline plots for $|\lambda| = 1$ reveal qualitatively steady Stokes behaviour near the particle surface and irrotational flow behaviour far from the particle. Pathlines, and thus convective processes, are dominated by the real component of the unsteady velocity field and are thus insensitive to particle geometry. It seems unlikely that small-amplitude oscillatory motion can significantly enhance mass transport between a fluid and suspended particles.

In general, the flow field past an oscillating particle will be asymmetric. Except for the special case of axisymmetric oscillations, the tangential traction has two components; stagnation points (curves) are thereby precluded. Asymmetric surface flow reversal is more complex (Loewenberg 1994). Except for initiation of the unsteady near-field flow reversal process, however, instantaneous streamline patterns, and thus pathlines, are similar for all particles. After surface flow reversal is complete, the remainder of the near-filed flow reversal process for any particle involves the formation of a single spherical eddy that expands according to (5.4). The far-field pressure and velocity fields are generally described by (5.1) and (5.3).

This work was supported by a grant from the Australian Research Council.

REFERENCES

ALLEGRA, J. R. & HAWLEY, S. A. 1971 Attenuation of sound in suspensions and emulsions: theory and experiments. *J. Acoust. Soc. Am.* **51**, 1545–1564.

BATCHELOR, G. K. 1967 *An Introduction to Fluid Dynamics.* Cambridge University Press.

BASSET, A. B. 1888 *A Treatise on Hydrodynamics*, vol. 2. Cambridge: Deighton Bell.

BURGERS, J. M. 1938 On the motion of small particles of elongated form suspended in a viscous liquid. Second report on viscosity and plasticity, Chap. III. *Kon. Ned. Akad. Wet.* **16**, 113–184.

CHAN, P. C., LEU, R. J. & ZARGAR, N. H. 1986 On the solution for the rotational motion of an axisymmetric rigid body at low Reynolds number with application to a finite length cylinder. *Chem. Engng Commun.* **49**, 145–163.

DAVIS, R. H. 1991 Sedimentation of axisymmetric particles in shear flows. *Phys. Fluids* A **3**, 2051–2060.

DEAN, W. R. & MONTAGNON, P. E. 1949 On the steady motion of viscous liquid in a corner. *Proc. Camb. Phil. Soc.* **45**, 389–394.

EDWARDES, D. 1892 Steady motion of a viscous liquid in which an ellipsoid is constrained to rotate about a principal axis. *Q. J. Maths* **26**, 70–78.

GAVZE, E. 1990 The accelerated motion of rigid bodies in non-steady Stokes flow. *J. Multiphase Flow* **16**, 153–166.

GHADDAR, N. K., MAGEN, M., MIKIC, B. B. & PATERA, A. T. 1986 Numerical investigation of incompressible flow in grooved channels. Part 2. Resonance and oscillatory heat-transfer enhancement. *J. Fluid Mech.* **168**, 541–567.

GLUCKMAN, M. J., WEINBAUM, S. & PFEFFER, R. 1972 Axisymmetric slow viscous flow past an arbitrary convex body of revolution. *J. Fluid Mech.* **55**, 677–709.

HEISS, J. F. & COULL, J. 1952 The effect of orientation and shape on the settling velocity of non-isometric particles in a viscous medium. *Chem. Engng Prog.* **48**, 133–140.

HESS, J. L. 1962 Calculation of potential flow about bodies of revolution having axes perpendicular to the free-stream direction. *J. Aerospace Sci.* **29**, 726–742.

HOCQUART, R. & HINCH, E. J. 1983 The long-time tail of the angular-velocity autocorrelation function for a rigid Brownian particle of arbitrary centrally symmetric shape. *J. Fluid Mech.* **137**, 217–220.

HURD, A. J., CLARK, N. A., MOCKLER, R. C. & O'SULLIVAN, W. J. 1985 Friction factors for a lattice of Brownian particles. *J. Fluid Mech.* **153**, 401–416.

JACKSON, J. D. 1962 *Classical Electrodynamics.* John Wiley & Sons.

JEFFERY, G. B. 1922 The motion of ellipsoid particles immersed in a viscous fluid. *Proc. R. Soc. Lond.* A **102**, 161–179.

KARRILA, S. J. & KIM, S. 1989 Integral equations of the second kind for the Stokes flow: direct solution for physical variables and removal of inherent accuracy limitations. *Chem. Engng Commun.* **82**, 123–161.

KASPER, G., NIIDA, T. & YANG, M. 1985 Measurements of viscous drag on cylinders and chains of spheres with aspect ratios between 2 and 50. *Aerosol. Sci.* **16**, 515–556.

KIM, S. & KARRILA, S. J. 1991 *Microhydrodynamics: Principles and Selected Applications.* Butterworth-Heinemann.

LADYZHENSKAYA, O. A. 1969 *The Mathematical Theory of Viscous Incompressible Flow.* Gordon & Breach.

LAWRENCE, C. J. & WEINBAUM, S. 1988 The unsteady force on a body at low Reynolds number; the axisymmetric motion of a spheroid. *J. Fluid Mech.* **189**, 463–489.

LOEWENBERG, M. 1993 The unsteady Stokes resistance of arbitrarily oriented, finite-length cylinders. *Phys. Fluids* A **5**, 3004–3006.

LOEWENBERG, M. 1994 Asymmetric, oscillatory motion of a finite-length cylinder: the macroscopic effect of particle edges. *Phys. Fluids* **6**, 1095–1107.

LOEWENBERG, M. & O'BRIEN, R. W. 1992 The dynamic mobility of nonspherical particles. *J. Colloid Interface Sci.* **150**, 158–168.

OBERBECK, A. 1876 Über stationäre Flüssigkeitsbewegungen mit Berücksichtigung der inneren Reibung (On steady-state flow under consideration of inner friction). *J. Reine. Angew. Math.* **81**, 62–80.

O'BRIEN, R. W. 1990 The electroacoustic equations for a colloidal suspension. *J. Fluid Mech.* **212**, 81–93.

POZRIKIDIS, C. 1989*a* A singularity method for unsteady linearized flow. *Phys. Fluids* A **1**, 1508–1520.

POZRIKIDIS, C. 1989*b* A study of linearized oscillatory flow past particles by the boundary-integral method. *J. Fluid Mech.* **202**, 17–41.

POZRIKIDIS, C. 1992 *Boundary Integral and Singularity Methods.* Cambridge University Press.

SMITH, A. M. O. & PIERCE, J. 1958 Exact solution of the Neumann problem. Calculation of plane and axially symmetric flow about or within arbitrary boundaries. *Proc. 3rd US Nat Congr. of Appl. Mech.*, pp. 807–815.

STOKES, G. G. 1851 On the effect of internal friction of fluids on the motion of pendulum. *Trans. Camb. Phil. Soc.* **9**, 8.

UI, T. J., HUSSEY, R. G. & ROGER, R. P. 1984 Stokes drag on a cylinder in axial motion. *Phys. Fluids* **27**, 787–795.

WILLIAMS, W. E. 1966 A note of slow vibrations in a viscous fluid. *J. Fluid Mech.* **25**, 589–590.

YOUNGREN, G. K. & ACRIVOS, A. 1975 Stokes flow past a particle of arbitrary shape: a numerical method of solution. *J. Fluid Mech.* **69**, 377–403.